

## Study on high-temperature oxidation of TiZrHfNbTaV high-entropy alloy

Zixuan Shangguan, Shuo Ma, Jun Li, Panmei Liu, Zumin Wang <sup>\*</sup>

School of Materials Science and Engineering, Tianjin University, Tianjin 300350, China



### ARTICLE INFO

#### Keywords:

High-entropy alloy  
Refractory  
Oxidation  
Complex oxides  
Microstructure

### ABSTRACT

The elemental effects and oxide layer evolutions of high-entropy alloys during oxidation have remained largely unclear. The high-temperature oxidation of equimolar refractory high-entropy alloy TiZrHfNbTaV in the air at 800–1000 °C for 1 h was investigated in terms of the oxide layer microstructure and formation mechanism. The non-dense oxides formed on the alloy surface at 800–1000 °C mainly contain TiNb<sub>2</sub>O<sub>7</sub>, providing favorable oxygen diffusion conditions. The growth of the oxide layer is influenced by the oxidation temperatures, free energy of oxides, and elemental segregation. The findings offer fundamental insights into the oxidation mechanism of the refractory high-entropy alloys.

### 1. Introduction

High-entropy alloys (HEAs) are an emerging class of materials that have attracted great attention due to their application potential [1–5]. Although many refractory HEAs exhibit excellent mechanical properties, they have poor oxidation resistance at high temperatures [6,7]. Adding Al and Cr elements will improve the oxidation resistance of the HEAs, but these elements tend to promote the formation of brittle intermetallic compounds [8,9]. Nb is detrimental to the oxidation resistance of HEA due to its high diffusivity [10]. Moreover, the formation of Ta<sub>2</sub>O<sub>5</sub> and Nb<sub>2</sub>O<sub>5</sub> does not provide any protection to the HEA [6,11]. Due to the limited attention to HEA oxidation, a systematic understanding of the oxidation mechanisms in HEAs has not been established, which greatly limits the potential application of HEAs [12–14].

Considering the above background, we prepared the TiZrHfNbTaV high-entropy alloy. In this paper, the oxidation resistance and oxide layer microstructure of the HEA at 800–1000 °C for 1 h are studied in detail. In addition, the element distribution and phase structure of the HEA oxide layer are also characterized.

### 2. Experimental

The equiatomic TiZrHfNbTaV high-entropy alloy was prepared by vacuum arc melting of a nominal mixture of pure elements (purity >99.9 wt%). Bulk specimens with a dimension of 6 × 6 × 1.5 mm<sup>3</sup> were prepared. Before oxidation, all faces of the specimens were polished by using abrasive papers (#80–#7000) and diamond polishing liquid (0.25

μm). The tube furnace was preheated to the target temperature before the specimens were introduced into the furnace. Air oxidation of the specimens was conducted at 800, 900, and 1000 °C for 1 h in a tube furnace (OTF-1200X, Hefei Kejing Materials Technology Co., Ltd.). After isothermal oxidation, the specimens were taken out of the furnace and cooled naturally.

The crystal structure of the alloy phases and oxidation products were identified by X-ray diffraction (XRD) on a Bruker D8 Advanced diffractometer. The morphology and elemental distribution of the surface and cross-section of oxidized specimens were studied using a scanning electron microscope (SEM, FEI Apreo S) equipped with an energy-dispersive spectrometer (EDS, Oxford X-MAX20).

### 3. Results and discussion

Fig. 1(a-b) shows the XRD patterns of the HEAs in the as-cast state and after oxidation for 1 h at 800–1000 °C. The HEA matrix has a body centered cubic (BCC) structure. In addition, the XRD pattern of Fig. S1 shows that the core of the specimen maintains the BCC structure at 1000 °C. The results indicate the high stability of the BCC single phase on the alloy substrate (Supplementary Material). The oxide layers of the alloys contain various complex oxides. The oxidized specimens have similar surface oxide phases at 800–1000 °C. TiNb<sub>2</sub>O<sub>7</sub>, Nb<sub>2</sub>Zr<sub>6</sub>O<sub>17</sub>, and Hf<sub>6</sub>Ta<sub>2</sub>O<sub>17</sub> are predominant, while HfO<sub>2</sub>, V<sub>3</sub>O<sub>5</sub>, Nb<sub>2</sub>O<sub>5</sub>, and TiO<sub>2</sub> are also detected. Previous studies have shown that some binary oxides react with each other to form more stable ternary oxides [11,15]. In this work, it has been found that the binary oxides of Ta and Hf can also react with each other to form Ta<sub>2</sub>Hf<sub>6</sub>O<sub>17</sub>.

\* Corresponding author.

E-mail address: [z.wang@tju.edu.cn](mailto:z.wang@tju.edu.cn) (Z. Wang).

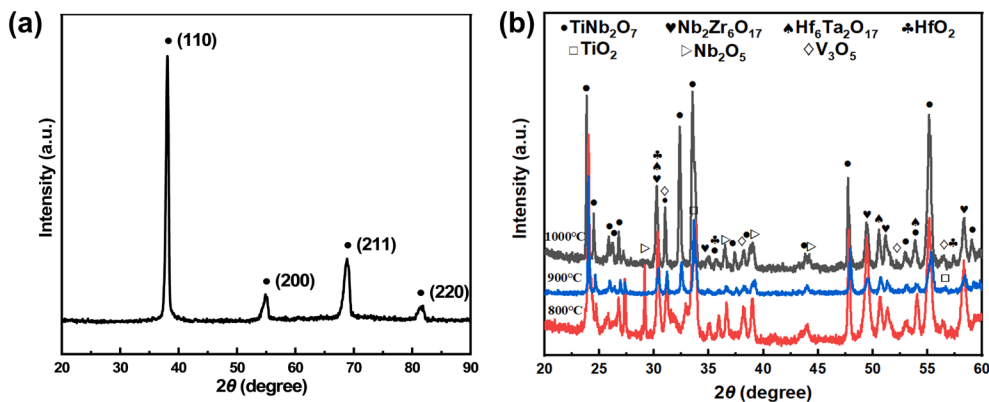


Fig. 1. (a) XRD pattern of the as-cast TiZrHfNbTaV. (b) XRD patterns of TiZrHfNbTaV oxidized at 800–1000 °C for 1 h.

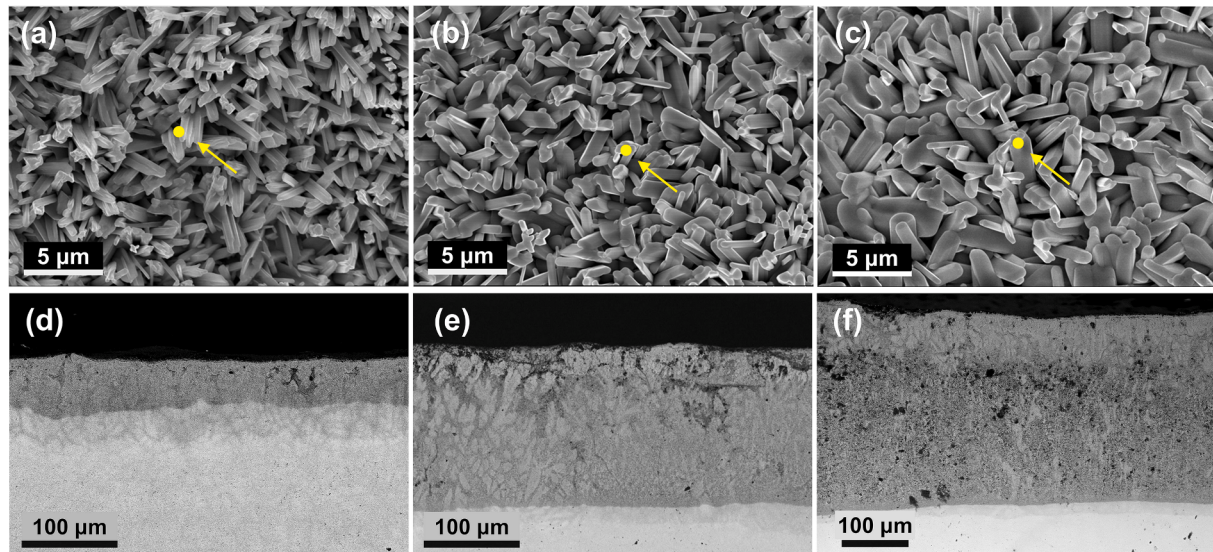


Fig. 2. SEM micrographs and cross-sectional SEM micrographs of the TiZrHfNbTaV specimens oxidized at (a, d) 800 °C, (b, e) 900 °C, and (c, f) 1000 °C for 1 h.

The surface morphologies and the cross-sectional SEM micrographs of the HEAs after oxidation at 800–1000 °C for 1 h are shown in Fig. 2. The surface oxide layers of the specimens consist of loose whisker-like structures, but they are not dense enough to prevent further diffusion of oxygen. Table S1 presents the chemical compositions of the surface oxides at 800–1000 °C determined by EDS. It follows that the surface oxides are rich in Nb and Ti, but depleted in Zr and Hf. The cross-section of the oxide layer at 800–1000 °C shows elemental segregation (Fig. 2(d–f)). The interaction between elements in the air (e.g., O and N) and those in the alloy can cause elemental segregation [16–18], which is related to the free energy of oxidation products and the diffusion rate of elements.

Fig. S2 shows the cross-sectional SEM micrographs and EDS of the oxide layer formed at 800 °C, indicating the enrichment of Nb and Ti in whisker-like oxides. Fig. 3 shows the cross-sectional SEM micrographs of the oxide layer at 900 °C. Ti has a strong oxygen affinity, and oxygen solubility in Nb is high [10,19]. Enriching Nb and Ti in the outermost oxide layer (see Fig. 3a) promotes the formation of  $\text{TiNb}_2\text{O}_7$ .  $\text{TiNb}_2\text{O}_7$  contains a high density of anion vacancies, and oxygen can be absorbed and diffused through the  $\text{TiNb}_2\text{O}_7$  to the alloy substrate [20]. Unlike the oxide layer formed at 800 °C, discontinuous dendrite-like structures beneath whisker-like oxides are located at the top of the oxide layer at 900 °C. Combined with EDS line scanning, this dendrite-like oxide is likely to be a mixture of  $\text{HfO}_2$  and  $\text{ZrO}_2$ . The standard Gibbs energies of formation (per mole  $\text{O}_2$ ) of different oxides at 900 °C follow the sequence:  $\text{HfO}_2 < \text{ZrO}_2 < \text{TiO}_2 < \text{Ta}_2\text{O}_5 < \text{Nb}_2\text{O}_5 < \text{V}_2\text{O}_5$  [15,21,22]. Ti

and Nb are briefly depleted below the Ti-Nb-rich whisker-like structures, and therefore  $\text{HfO}_2$  enriches the oxide. Previous studies have shown that Hf and Zr can form highly stable but brittle oxides ( $\text{Hf, Zr})_2\text{O}_2$  [23,24]. As a result,  $(\text{Hf, Zr})_2\text{O}_2$  in the oxide layer is susceptible to the formation of microcracks and pores under stress generated by the growth of surrounding various oxides. The EDS mappings in Fig. 3a show a lower concentration of V in the surface region of the oxide layer, which may be due to the volatilization of  $\text{V}_2\text{O}_5$  ( $\text{V}_2\text{O}_5$  has strong volatility above 690 °C [25]).

Elemental segregation zones are the main organization of the oxide layer at 900 °C in Fig. 3c. The oxide layer is composed of seemingly periodic structures. In this structure, Ti and V tend to aggregate, Nb and Ta tend to aggregate, and Zr and Hf tend to aggregate. The substitution of elements from the same periodic group is likely: Nb and Ta, Zr and Hf have similar crystal structures, atomic radius ( $r$ ), melting point ( $T_m$ ) and electronegativity (see Table S2) [26]. However, extensive elemental segregation indicates that a continuous oxide layer cannot be formed on the surface of the alloy to prevent oxygen from entering the alloy substrate.

The specimen oxidized at 1000 °C is successively composed of an oxide layer, an oxidation-affected region and the alloy substrate as shown in Fig. 4a. The oxide layer contains an outer oxide layer and an inner oxide layer. Fig. 4b shows the whisker-like structure at the top of the oxide layer with a Zr-Hf-rich dendrite-like structure below it.  $(\text{Hf, Zr})_2\text{O}_2$  presents a dendrite-like morphology, which is the result of the stable

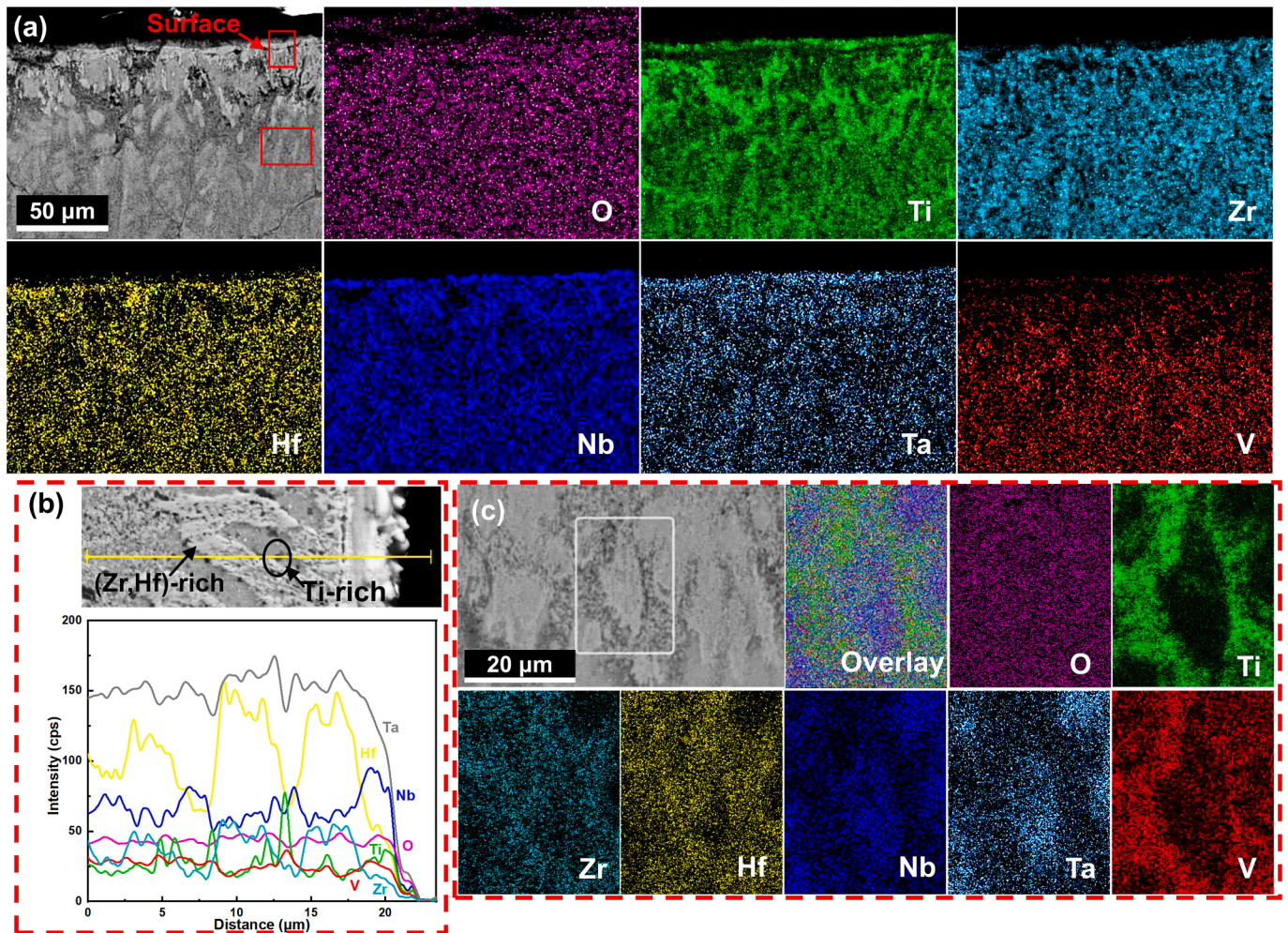


Fig. 3. Cross-sectional SEM micrograph and EDS mapping of the TiZrHfNbTaV specimen oxidized at (a) 900 °C for 1 h. (b) The EDS line scanning at the top of the oxide layer. (c) The EDS mapping of local area in the 900 °C oxide layer. The SEM micrographs of (b) and (c) are captured from the areas inset by red boxes in (a).

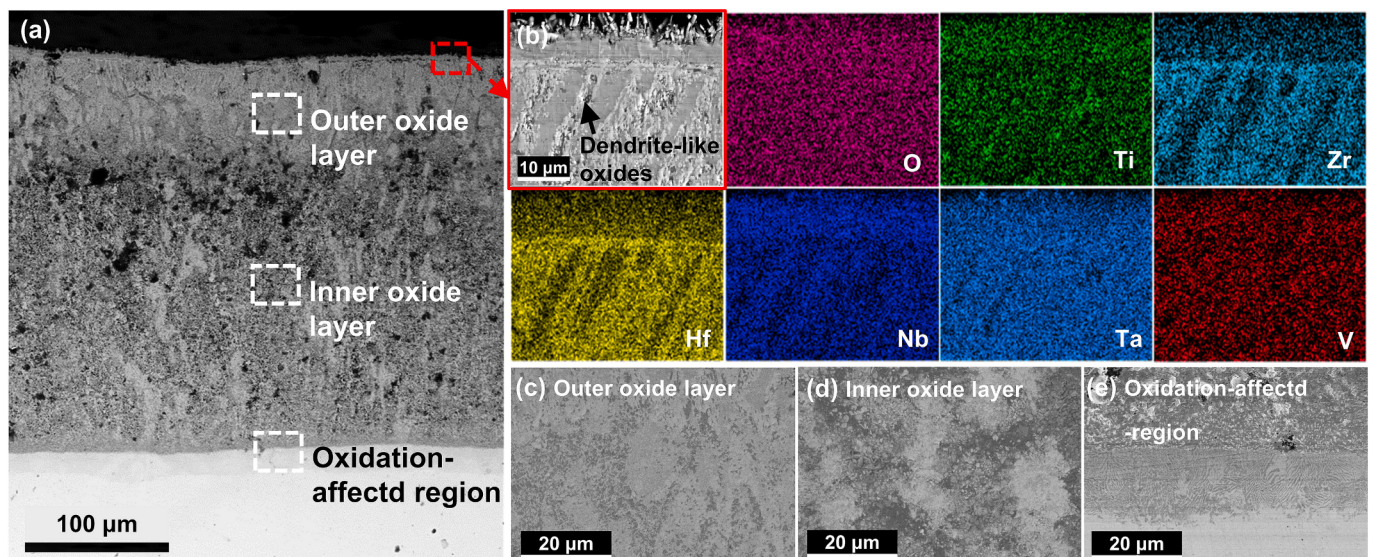


Fig. 4. Cross-sectional SEM micrograph of the TiZrHfNbTaV specimen oxidized at (a) 1000 °C for 1 h. High magnification cross-sectional SEM micrograph and EDS mapping of the top of the oxide layer formed by oxidation at (b) 1000 °C for 1 h. The SEM micrographs of (c), (d), and (e) are captured from the areas inset by white boxes in (a).

stack of Hf, Zr, and O atoms along a certain crystal orientation [20]. The outer oxide layer of the HEAs formed at 1000 °C (Fig. 4c) is similar to the oxide layer at 900 °C. The low density and high porosity of the inner oxide layer formed at 1000 °C (Fig. 4d) make it easier for oxygen to penetrate towards the substrate.

#### 4. Conclusions

In this work, the oxidation behaviors of TiZrHfNbTaV high-entropy alloy after oxidation in air at 800–1000 °C for 1 h were studied. Oxides such as  $TiNb_2O_7$ ,  $Nb_2Zr_6O_{17}$ , and  $Hf_6Ta_2O_{17}$  are formed on the surface of the alloy at 800–1000 °C.  $TiNb_2O_7$  at the top of the oxide layer cannot restrain the inward migration of oxygen from the air. The brittle dendrite-like  $(Hf, Zr)O_2$  formed above 900 °C tends to cause pores in the oxide layer. At 1000 °C, the pores of the inner oxide layer served as places for accelerated oxygen ingress toward the substrate. In addition, elemental segregation reduces the oxidation resistance of the HEAs. The above findings provide a new understanding for developing oxidation-resistant refractory high-entropy alloys.

#### CRediT authorship contribution statement

**Zixuan Shangguan:** Investigation, Methodology, Writing – original draft. **Shuo Ma:** Investigation, Validation. **Jun Li:** Methodology, Visualization. **Panmei Liu:** Data curation, Formal analysis. **Zumin Wang:** Project administration, Supervision, Writing – review & editing.

#### Declaration of competing interest

The authors declare that they have no known competing financial interests or personal relationships that could have appeared to influence the work reported in this paper.

#### Data availability

Data will be made available on request.

#### Acknowledgements

This work was supported by the National Natural Science Foundation of China (No. 51971153).

#### Appendix A. Supplementary data

Supplementary data to this article can be found online at <https://doi.org/10.1016/j.matlet.2024.135907>.

#### References

- [1] N. Yurchenko, E. Panina, A. Belyakov, G. Salishchev, S. Zherebtsov, N. Stepanov, Mater. Lett. 311 (2022) 131584.
- [2] X. Ren, Y. Li, Y. Qi, B. Wang, Materials 15 (2022) 2931.
- [3] N. Yurchenko, E. Panina, S. Zherebtsov, N. Stepanov, Corros. Sci. 205 (2022) 110464.
- [4] J.W. Yeh, S.K. Chen, S.J. Lin, J.Y. Gan, T.S. Chin, T.T. Shun, C.H. Tsau, S.Y. Chang, Adv. Eng. Mater. 6 (2004) 299–303.
- [5] Z.Q. Xu, Z.L. Ma, Y. Tan, X.W. Cheng, Scripta Mater. 206 (2022) 114230.
- [6] S. Lu, X. Li, X. Liang, W. Yang, J. Chen, Metals. 12 (2021) 41.
- [7] S. Zhang, W. Qi, R. Zhang, Mater. Lett. 345 (2023) 134490.
- [8] J. Wen, X. Chu, Y. Cao, N. Li, Metals. 11 (2021) 514.
- [9] O.A. Waseem, H.J. Ryu, J. Alloys Compd. 828 (2020) 154427.
- [10] R.A. Perkins, G.H. Meier, JOM 42 (1990) 17–21.
- [11] O.N. Senkov, J. Gild, T.M. Butler, J. Alloys Compd. 862 (2021) 158003.
- [12] S. Shahajan, A. Kumar, M. Chopkar, A. Basu, Mater. Res. Express. 7 (2020) 016532.
- [13] R. Gawel, Ł. Rogal, K. Przybylski, J. Mater. Eng. Perform. 28 (2019) 4163–4170.
- [14] C.H. Chang, M.S. Titus, J.W. Yeh, Adv. Eng. Mater. 20 (2018) 1700948.
- [15] T.M. Butler, K.J. Chaput, J.R. Dietrich, O.N. Senkov, J. Alloys Compd. 729 (2017) 1004–1019.
- [16] A. Kashyap, B. Vishwanad, A. Chauhan, S.R. Meka, Acta Mater. 263 (2024) 119523.
- [17] S.A.R. Qadri, K.N. Sasidhar, B. Vishwanad, S.R. Meka, Acta Mater. 263 (2024) 119532.
- [18] R. Su, H. Zhang, G. Ouyang, L. Liu, D.D. Johnson, J.H. Perepezko, Acta Mater. 246 (2023) 118719.
- [19] D.E. Poland, A.K. Kuriakose, J.L. Margrave, J. Phys. Chem. 69 (1965) 158–160.
- [20] D. Ouyang, Z.J. Chen, H.B. Yu, K.C. Chan, L. Liu, Corros. Sci. 198 (2022) 110153.
- [21] L. Backman, J. Gild, J. Luo, E.J. Opila, Acta Mater. 197 (2020) 20–27.
- [22] B. Gorr, S. Schellert, F. Müller, H.J. Christ, A. Kauffmann, M. Heilmairer, Adv. Eng. Mater. 23 (2021) 2001047.
- [23] S. Zhang, R. Li, Y. Xu, Mater. Res. Express. 9 (2022) 096510.
- [24] S. Zhang, X. Guo, Mater. Sci. Eng. A 638 (2015) 121–131.
- [25] D.B. Lee, Met. Mater. Int. 11 (2005) 141–147.
- [26] L. Backman, J. Gild, J. Luo, E.J. Opila, Acta Mater. 197 (2020) 81–90.